Journal of Fluids and Structures 27 (2011) 1111–1123

Contents lists available at ScienceDirect

Journal of Fluids and Structures

journal homepage: www.elsevier.com/locate/jfs

Drag reduction by reconfiguration of a poroelastic system

Frédérick P. Gosselin, Emmanuel de Langre *

Département de Mécanique, Ladhyx-CNRS, École Polytechnique, 91128 Palaiseau, France

A R T I C L E I N F O

Article history:
Received 1 July 2010
Accepted 9 May 2011
Available online 17 June 2011

Keywords:
Reconfiguration
Drag reduction
Poroelasticity
Large amplitude deformation

A B S T R A C T

Because of their flexibility, trees and other plants deform with great amplitude (reconfigure) when subjected to fluid flow. Hence the drag they encounter does not grow with the square of the flow velocity as it would on a classical bluff body, but rather in a less pronounced way. The reconfiguration of actual plants has been studied abundantly in wind tunnels and hydraulic canals, and recently a theoretical understanding of reconfiguration has been brought by combining modelling and experimentation on simple systems such as filaments and flat plates. These simple systems have a significant difference with actual plants in the fact that they are not porous: fluid only flows around them, not through them. We present experimentation and modelling of the reconfiguration of a poroelastic system. Proper scaling of the drag and the fluid loading allows comparing the reconfiguration regimes of porous systems to those of geometrically simple systems. Through theoretical modelling, it is found that porosity affects the scaling of the drag with flow velocity. For high porosity systems, the scaling is the same as for isolated filaments while at low porosity, the scaling is constant for a large range of porosity values. The scalings for the extreme values of porosity are also obtained through dimensional analysis.

1. Introduction

Phenomena of fluid–structure interactions are ubiquitous in vegetation due to the great flexibility of plants (de Langre, 2008). For example, wind causes waves on the surface of wheat fields (Py et al., 2006), the blades of giant kelp squeeze into tight bundles when subjected to tidal flow (Koehl and Alberte, 1988), and the leaves of poplar trees flutter at the slightest breeze (Niklas, 1991). The great flexibility of plants comes as the solution to an optimisation problem plants face: that of maximising surface area and height to capture sunlight with a finite quantity of material (Vogel, 1984).

In this paper, we are specifically concerned with the static drag of plants and how their flexibility allows for a minimisation of the stresses encountered. It is essential to understand the fluid loadings on vegetation in order to devise better models to comprehend and predict wind damages to forests (Dupont and Brunet, 2006), crops (Baker, 1995) and shore vegetation (Boizard and Mitchell, 2009), as well as to study the adaptation of aquatic and terrestrial plants to their environment.

The problem of the drag of vegetation is complicated by the fact that when subjected to fluid flow, trees and other plants deform with great amplitude because of their flexibility. Through deformation, plants encounter fluid loadings much smaller than if they were rigid (Vogel, 1996). We say that they *reconfigure* (Vogel, 1984), i.e., they reduce their cross-sectional area and become more streamlined. To quantify the effect of reconfiguration on drag reduction, we use the Vogel

* Corresponding author.
E-mail addresses: frederick.gosselin@ladhyx.polytechnique.fr (F.P. Gosselin), delangre@ladhyx.polytechnique.fr (E. de Langre).

0889-9746/$ - see front matter © 2011 Elsevier Ltd. All rights reserved.
doi:10.1016/j.jfluidstructs.2011.05.007

exponent $\mathcal{V}$ which expresses the deviation from the classical scaling law of a rigid bluff body

$$F \propto U_\infty^{2+\mathcal{V}}, \tag{1}$$

where F is the drag load and U_∞ is the flow velocity. For example, the leaf of the tulip tree rolls up into a cone when subjected to increasing wind speed (Vogel, 1989) hence decreasing its cross-sectional area and becoming more streamlined. This reconfiguration has for effect that the drag on the leaf increases more or less linearly with flow speed ($\mathcal{V} \sim -1$). The reconfigurations of many species of plants have been studied in wind tunnels, tow tanks and hydraulic canals. Collections of measures of reconfiguration and Vogel exponents for various species can be found in Vogel (1996, p. 143) as well as Harder et al. (2004). Moreover, some man made structures do experience drag reduction due to large amplitude reconfiguration such as aquaculture net cages (Moe et al., 2010).

Recently a more fundamental understanding of the mechanisms of reconfiguration has been brought by combining modelling and experimentation on simple systems such as filaments and flat plates (Shelley and Zhang, 2011). Alben et al. (2002, 2004) studied the reconfiguration of a flexible filament supported at its centre in a 2-D soap film flow. The drag reduction and the bending deformation of the filament measured experimentally were properly modelled with a potential flow theory coupled with a Euler–Bernoulli beam formulation. From their experimental and theoretical results (Alben et al., 2004) concluded that the scaling of the drag of the fibre transitioned from a rigid regime ($\mathcal{V}=0$) to a large deformation regime with $\mathcal{V}=-\frac{2}{3}$ as the hydrodynamic force was increased with respect to the rigidity of the fibre.

Gosselin (2009) and Gosselin et al. (2010) compared drag measurements of flexible thin plates in a wind tunnel with predictions from a simplified model based on an empirical drag formulation. The simplified model predicts well the reconfiguration of plates and further comparisons showed that the reconfiguration of a rectangular flexible plate supported at its centre in a wind tunnel is identical to that of a filament in a soap film as studied by Alben et al. (2002, 2004). Moreover, Gosselin et al. (2010) showed that in the regime of large deformation, the scaling of the drag with the flow velocity can be deduced by dimensional analysis through the assumption that for a very deformed system, the original characteristic length becomes irrelevant. Consider the 2-D reconfiguration of an elastic system with drag per unit width F/W and bending rigidity per unit width EI/W subjected to a fluid flow of velocity U_∞ and density ρ. If it is assumed that the elastic body is so deformed that its original length ℓ is irrelevant, the four quantities can be combined into a single dimensionless number required to describe the problem:

$$\frac{F}{W(EI/W)^{1/3}\rho^{2/3}U_\infty^{4/3}}.$$

From this dimensionless number, the scaling $F \propto U_\infty^{4/3}$ and equivalently the Vogel exponent $\mathcal{V}=-\frac{2}{3}$ can be deduced, in agreement with the potential flow theory of Alben et al. (2004).

Schouveiler and Boudaoud (2006) explored the 3-D reconfiguration of a circular flat plate cut along a radius and supported at its centre. When subjected to water flow, the circular plate rolled up into a cone which became tighter as the flow rate was increased similarly to the tuliptree leaf of Vogel (1989). The drag and reconfiguration of the circular plates of Schouveiler and Boudaoud (2006) was well matched by the predictions of a simplified momentum conservation model. Moreover, this model predicted that in the large deformation regime, the scaling of the drag with flow velocity should obey a Vogel exponent of $\mathcal{V}=-\frac{4}{3}$ while Gosselin et al. (2010) obtained that same value with a dimensionless analysis similar to the one discussed above applied to the 3-D reconfiguration of a flat plate.

The study of the reconfiguration of idealised systems allowed understanding the basic mechanisms of drag reduction affecting trees and vegetation. However, a major difference separates beams and plates from actual trees: fluid must flow *around* simple obstacles while wind flows *trough* a porous structure such as a tree. The elements composing the plants like the leaves and the branches perceive an effective flow velocity modified from that of the free stream velocity. Because the plant is a poroelastic system, when reconfiguring, it modifies this effective flow velocity.

Modelling this type of poroelastic structures has recently gained a lot of attention for all sorts of applications. Py et al. (2006) as well as Dupont et al. (2010) used an averaging technique to model the drag force of a swaying crop canopy as a volumetric force coupled with the momentum conservation equations of the flow. Similarly, Favier et al. (2009) modelled the effect of a passively deforming homogeneous layer of hairlike structures on the fluctuating drag of a bluff body and Ricciardi et al. (2009) studied the non-linear stability of a nuclear reactor core.

The goal of the present paper is thus to characterise the effect on reconfiguration of poroelasticity. Extensive wind tunnel testing was realised on poroelastic bodies as well as flexible filaments. These experimental results allow us to define a proper Cauchy number which governs the problem of reconfiguration and accounts for geometry, Reynolds and porosity effects. Moreover, with a simple theoretical model for the reconfiguration of the poroelastic system studied, we investigate the mechanisms of drag reduction and study the effect of porosity on reconfiguration. A dimensional analysis is presented to obtain the scaling of the drag with flow velocity for poroelastic bodies in the large deformation regime.

2. Experiments

To understand the effect of porosity on the problem of reconfiguration, we performed experiments in a wind tunnel to measure the drag of simple filaments as well as that of poroelastic bodies.

2.1. Methodology

We measured the drag of flexible cylindrical filaments of diameter d, length ℓ and flexural rigidity EI (Fig. 1). Three specimens of filaments supported at their centre were tested, their properties are given in Table 1. Because the filaments were small and had little drag, 50 identical filaments were mounted on a specially designed support to test them in the wind tunnel (Fig. 2). A significant measure of drag could thus be obtained. The spacing between the filaments on the support was of 10 diameters in the transverse direction and 40 diameters in the streamwise direction. The interaction between filaments is thus neglected. To avoid a bidimensional deformation, the filaments were mounted vertically in the wind tunnel. Hence, the lower half of a filament is rigidified by gravity and the upper half is effectively more flexible. On the whole filament, the effect of gravity is compensated and thus lessened. Regardless, at high flow velocity, aerodynamic loading becomes much larger than weight. In addition to the three flexible filaments, rigid cylinders of the same dimensions were tested.

The poroelastic system studied is a ball of diameter D made of N round filaments of diameter d tied together at the center of the ball (Fig. 3). The core of the ball where all the filaments are tied is relatively rigid and has a diameter D_i. The ball is screwed onto a downstream support which transmits the drag force to the force sensor. The specimens were manufactured by Hasbro and sold as toys under the name of “Koosh balls”. The flexural rigidity EI of the filaments forming the ball was found by measuring the natural frequency of a single cantilever filament using a high-speed camera. Two poroelastic specimens were tested in the wind tunnel, their characteristics are given in Table 2. Moreover, a rigid porous specimen built with finishing nails planted in a styrofoam ball was tested (Fig. 4).

These laboratory experiments were conducted in a small Eiffel wind tunnel with a test section of 0.180 m $\times$ 0.180 m. The wind stream is produced by a centrifugal fan mounted downstream and exhausting air vertically. The mean velocity in the test section can be varied from 5 to 30 m/s with a turbulence level of 1.5% at 10 m/s.

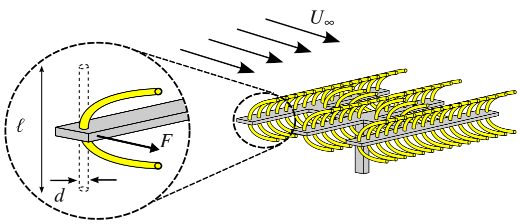

Fig. 1. Schematic diagram of the support holding 50 identical filaments and details of one filament.

Table 1
Parameter values of the tested flexible filaments and rigid cylinders.

	ℓ (cm)	d (cm)	EI/d (10^{-6} N m)
f1	4.0	0.094	127
f2	7.4	0.094	127
f3	11.6	0.094	127
c1	4.0	0.094	–
c2	7.4	0.094	–
c3	11.6	0.094	–

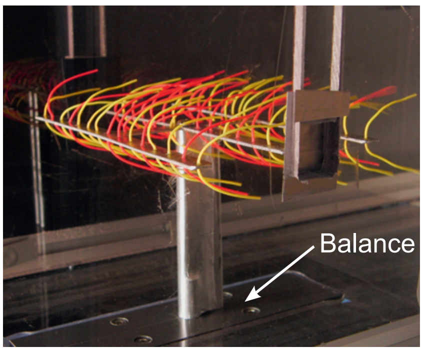

Fig. 2. Photograph of the support holding 50 filaments of length $\ell = 7.4$ subjected to an air flow of 20 m/s.

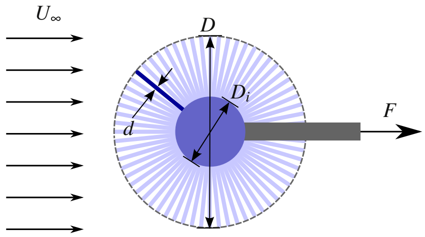

Fig. 3. Schematic of the poroelastic system.

Table 2
Parameter values of the tested flexible and rigid porous specimens.

	D (cm)	D_i (cm)	d (cm)	EI/d (10^{-6} N m)	N
FP1	8.9	3.1	0.094	127	900
FP2	5.4	1.6	0.068	38.1	1150
RP	8.9	3.0	0.09	–	530

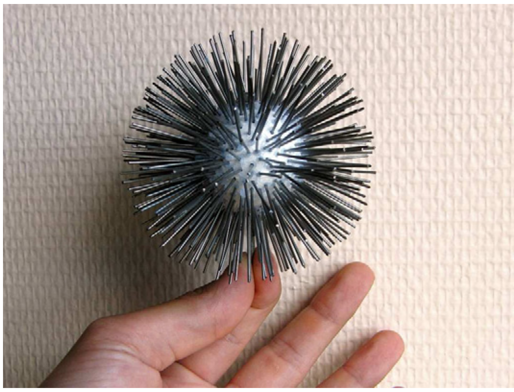

Fig. 4. Photograph of the rigid porous specimen. It has the same dimensions as the first poroelastic specimen, but is made of less cylinders (N=530).

The different specimens tested were mounted on a support connected to a five-axis force sensor located under the wind tunnel. The force sensor measured the drag of the specimen and a pitot-static system measured the flow velocity. For every specimen at each flow velocity tested, the 24 bit data acquisition system collected the measurements of the drag and the flow velocity for one minute and time-averaged the values. The drag on the support alone was measured and subtracted from the drag of each specimen.

2.2. Reconfiguration and drag measurements

The deformation of the first poroelastic specimen (FP1) is shown in Fig. 5 for three flow velocities. At 5 m/s (Fig. 5(a)), the deformation is small. As the flow velocity is increased further, the deformation becomes important and the filaments bend with the flow. Note that on Fig. 5(b), a dynamic coherent movement of the filaments blurs the picture. We presume that these coherent movements are due to a passive response of the filaments to vortex shedding on the ball. At 14 m/s, the standard deviation of the drag measurement fluctuations is less than 8% of the time-averaged value. For this reason, in this study of static reconfiguration, we neglect any dynamic effect due to vortex shedding, turbulence or other coupling mechanisms.

The drag measurements of the filaments and the rigid cylinders are shown on Fig. 6(a) while those for the three porous specimens are shown on Fig. 6(b). For both the cylinders and the porous systems, the increase of drag with flow velocity on the rigid specimens is almost quadratic. However, the drag of all flexible specimens has a smaller dependence on the flow velocity.

To analyse the effect of flexibility on drag, we must first characterise the drag of the rigid benchmark specimens. We define a drag coefficient and a Reynolds number for the rigid cylinders $C_D = 2F/\rho d\ell U_\infty^2$ and $\mathrm{Re} = \rho d U_\infty/\mu$ where F is the measured drag force, U_∞ is the flow velocity and ρ and μ are the fluid density and dynamic viscosity, respectively.

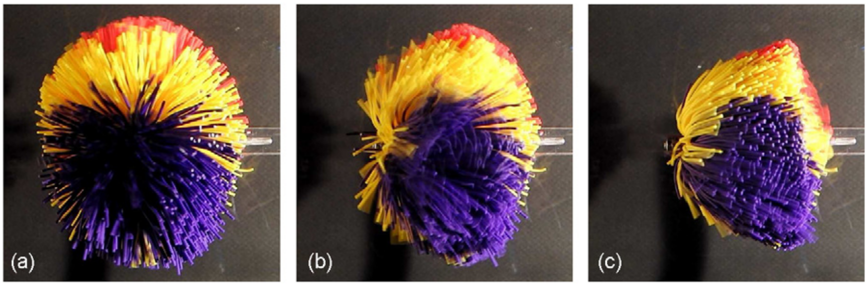

Fig. 5. Photographs of the deformation of the first poroelastic specimen in the wind tunnel at flow velocities of: (a) 5, (b) 14 and (c) 29 m/s.

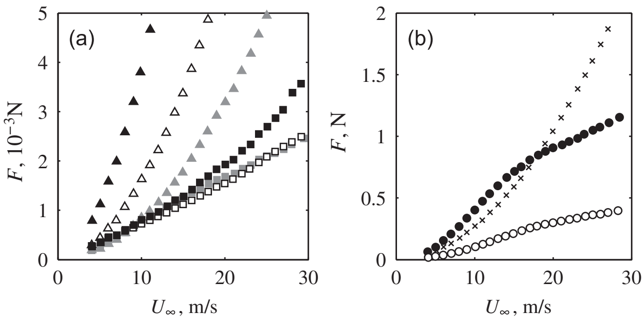

Fig. 6. Drag of (a) flexible filaments and rigid cylinders and as well as (b) porous specimens: ■, f1; ▲, c1; □, f2; △, c2; ■, f3; ▲, c3; •, FP1; ◦, FP2 and × RP.

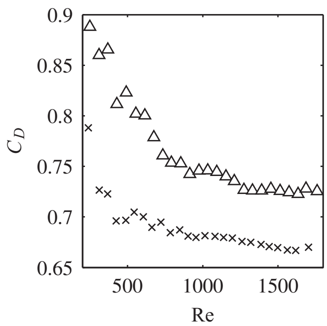

Fig. 7. Dependence of the drag coefficients on Reynolds number: ×, rigid porous specimen and △, rigid cylinder c2.

Similarly for the rigid porous specimen, we define a drag coefficient $C_D = 8F/\pi\rho D^2 U_\infty^2$ and use the same definition of Reynolds number based on the diameter of a cylinder of the porous ball. On Fig. 7, the drag coefficient of the rigid cylinders c2 as well as that of the rigid porous ball are shown in function of the Reynolds number. The effect of varying Reynolds number on the drag coefficient is similar for a single cylinder as for a porous ball made of 530 cylinders. By extrapolating, we could expect the effect of varying Reynolds number to be the same on a ball of 530, 900 or 1150 cylinders in the limit where the porosity of the system is still large. Under this assumption, we know how the drag on rigid porous balls equivalent to the poroelastic specimens studied varies and can thus isolate the effect of flexibility on the drag variation as the flow velocity is varied. To extract from the drag measurements the variations due to flexibility and thus fully appreciate the effect of reconfiguration, we develop appropriate dimensionless numbers.

2.3. Dimensionless numbers

We consider the drag F of a flexible slender cylindrical filament of length ℓ, diameter d and flexural rigidity EI bending due to a fluid flow of density ρ and velocity U_∞. We express this problem using the Cauchy number and the reconfiguration number:

$$\widetilde{C_Y} = C_D \frac{\rho \ell^3 U_\infty^2 d}{16EI}, \quad \mathcal{R} = \frac{F}{\frac{1}{2}\rho C_D \ell d U_\infty^2}. \tag{2}$$

The Cauchy number characterises the reconfiguration of an elastic medium subjected to flow (Cermak and Isyumov, 1998; Chakrabarti, 2002; de Langre, 2008; Gosselin et al., 2010). It is equal to the ratio of the aerodynamic force produced by the fluid on the original shape of the structure over the rigidity of the structure. We use the definition introduced by Gosselin et al. (2010) which includes the drag coefficient. This allows to take into account effects of geometry and Reynolds number. The reconfiguration number $\mathcal{R}$ emphasises the effect of flexibility on the drag by comparing the drag of the flexible filament to that of an equivalent rigid cylinder at the same Reynolds number.

For the poroelastic system, similar Cauchy and reconfiguration numbers can be defined based on the cross-sectional area of the ball. A new quantity, the surface density, is introduced

$$\widetilde{C_Y} = C_D \frac{\rho(D-D_i)^3 U_\infty^2 d}{16EI}, \quad \mathcal{R} = \frac{8F}{\rho\pi D^2 C_D U_\infty^2}, \quad \eta = \frac{Nd\frac{D}{2}}{\frac{1}{4}\pi D^2} = \frac{2Nd}{\pi D}. \tag{3}$$

We define the surface density as the ratio of the cross-sectional area of all the components of the porous body (the N filaments composing the ball) over the cross-sectional area of the undeformed poroelastic body.

The variation of $\mathcal{R}$ as function of $\widetilde{C_Y}$ is shown in Fig. 8 for the three specimens of filaments (□). The new experimental points are shown along with the results of Gosselin et al. (2010) on flexible rectangular plates (⁎) and those of Alben et al. (2002) on flexible fibres in a soap film flow (◆). Despite the different geometries, dimensions, rigidity and type of flow, all the data points collapse on a single curve. This confirms that the problems of reconfiguration of a filament and a rectangular plate in a wind tunnel, as well as a fibre in a soap film flow are essentially the same problem, i.e., the same dimensionless numbers characterise them and their reconfiguration is the same. Note that only the experimental points of Gosselin et al. (2010) and Alben et al. (2002) where blockage of the test section was minimal where used otherwise the reconfiguration is altered. Also note that superposition is only possible with the use of the Cauchy number definition of Eq. (2) which includes the drag coefficient C_D. Values of C_D for the different specimens plotted in Fig. 8 vary from 0.7 for the shortest filaments at the highest Reynolds number to 7 for the fibres in the soap film flow. The inclusion of the drag coefficient in the Cauchy number allows to fully isolate effects of flexibility on the drag from Reynolds number and geometry effects. For the sake of comparison, the reconfiguration curve predicted by the model of Gosselin et al. (2010) which couples an empirical drag formulation to the large deformation of a Euler–Bernoulli beam is shown in solid line in Fig. 8. The agreement between the experiments and the model is very good, and for this reason, the model is extended to poroelastic systems in the following section.

The Cauchy number governs the problem of the reconfiguration of slender systems (Fig. 8). For small values of $\widetilde{C_Y}$, the points are aligned on a horizontal line which indicates that the drag on the flexible objects varies as it would on a rigid object. At values of $\widetilde{C_Y}$ between 1 and 10, the reconfiguration number starts to decline as the specimens deform. As $\widetilde{C_Y}$ increases further, the decline of $\mathcal{R}$ seems to follow a constant logarithmic slope. Upon fitting a least square power law on the data points of Fig. 8 where $\widetilde{C_Y} > 100$, one finds that $\mathcal{R} \propto \widetilde{C_Y}^{-0.29}$ which corresponds to $F \propto U_\infty^{1.42}$ or $\mathcal{V} = -0.58$. This value of Vogel exponent is in agreement with the dimensional analysis of Gosselin et al. (2010) which predicts a Vogel exponent of $\mathcal{V} = -2/3$ based on the assumption that the characteristic length of the original undeformed system becomes irrelevant as presented in the introduction.

The reconfiguration curves for the first (•) and the second (◦) flexible porous specimens are shown on Fig. 9. The two curves are superimposed indicating that the Cauchy number is appropriate to describe the problem.

Differently from the reconfiguration of slender bodies in Fig. 8, the reconfiguration number of the poroelastic balls in Fig. 9 increases slightly before decreasing. At $\widetilde{C_Y} \approx 10$, the drag of the poroelastic balls is 18% larger than that of identical

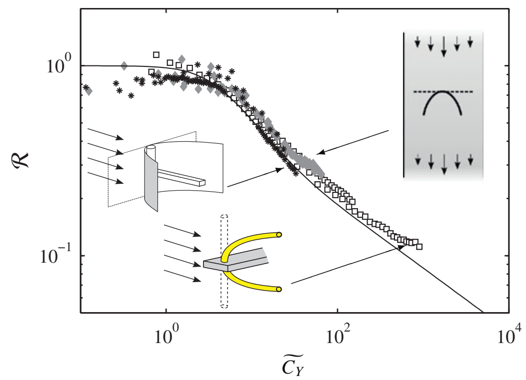

Fig. 8. Superposition of the experimental measurements of drag on flexible slender systems: □, three flexible filaments tested in a wind tunnel; ⁎, five rectangular plates tested in a wind tunnel by Gosselin et al. (2010); ◆, two fibres tested in a soap film flow by Alben et al. (2002) and —— the theoretical model of Gosselin et al. (2010).

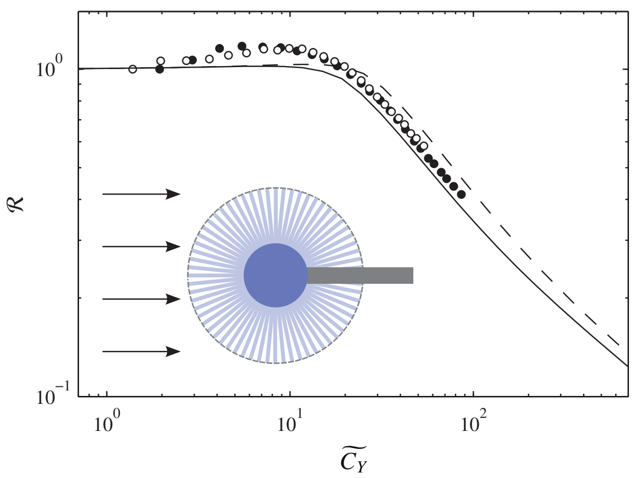

Fig. 9. Variation of the drag reduction of the poroelastic systems for increasing Cauchy number: •, first flexible specimen and ◦, second flexible specimen. The curves predicted by the theoretical model of Eqs. (13)–(15) are also shown: ——, first specimen with $\eta = 6.1$ and – – –, second specimen with $\eta = 9.2$.

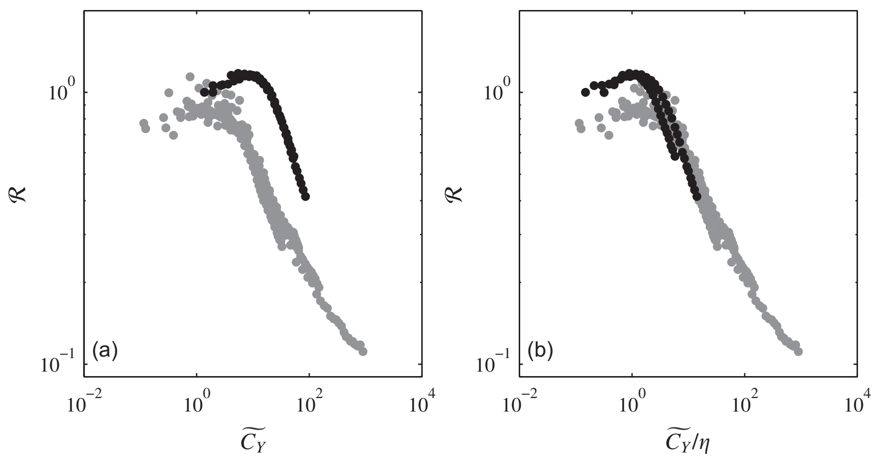

Fig. 10. Collapse of the reconfiguration curves of porous (•) specimens as well as the slender specimens (filaments, rectangular plates, fibres, ●) when plotted in function of: (a) the Cauchy number alone $\widetilde{C_Y}$ and (b) the Cauchy number divided by the surface density $\widetilde{C_Y}/\eta$.

rigid porous balls. This can be explained by the fact that the filaments which point upstream in the flow before the ball is deformed must adopt a position where they are more or less perpendicular to the flow before bending downstream with the flow (see Fig. 5(b)). Because of this, they significantly increase their drag. Some tree branches have been observed to exhibit the same phenomenon (Vogel, 1984).

Another noticeable difference between Figs. 8 and 9, is that the drag reduction begins at $\widetilde{C_Y} \approx 3$ for the plates, fibres and filaments while $\mathcal{R}$ only starts to decrease beyond $\widetilde{C_Y} \approx 20$ for the porous systems. The reconfiguration curve for the porous systems is shifted to higher values of $\widetilde{C_Y}$. This difference is highlighted in Fig. 10(a) where $\mathcal{R}$ is plotted for the slender specimens (●) along with the poroelastic specimens (•) versus the Cauchy number. In Fig. 10(b), the reconfiguration of both types of systems is plotted in function of the quotient of the Cauchy number by the surface density $\widetilde{C_Y}/\eta$. For the slender specimens, $\eta = 1$ while for the first and second poroelastic specimens it can be calculated from Eq. (3) with the data from Table 2 to be, respectively, $\eta = 6.1$ and $\eta = 9.2$. Dividing the Cauchy number by the surface density amounts to dividing the aerodynamic load evenly on all the structural elements composing the porous bodies.

For both porous and non-porous bodies, it is found that drag reduction begins at values of $\widetilde{C_Y}/\eta$ between 1 and 3. The curves are not collapsed as their slopes on the logarithmic plot are different. However, the starting points of the drag reduction of all systems studied are coalesced onto a point at $\widetilde{C_Y}/\eta$ between 1 and 3. It is shown with the following theoretical model that this coalescence of the drag reduction starting point can be extended on a much greater scale of surface density values.

3. Theoretical model

3.1. Model derivation

We consider the deformation of a ball made up of a collection of N identical cylindrical beams uniformly spread and clamped at the centre of the ball (Fig. 11(a)). The beams each have a bending rigidity EI, diameter d, length $D/2$ and form a ball of diameter D. This system is subjected to a flow of uniform velocity U_∞ of an inviscid fluid of density ρ.

The schematic diagram of beam j part of the system along with the flow it perceives are shown in Fig. 11(b). The undeformed beam j makes an angle Θ_j with the flow and has an azimuthal angle φ_j about the axis of the flow (Fig. 11(a)). The lagrangian coordinate S_j is defined along the central axis of this beam from its clamped end to its free end. The deformed shape of beam j is given by the local angle $\theta_j(S_j)$ the beam makes with the flow.

We use an empirical formulation of the fluid forces based on the model of Gosselin et al. (2010). As in their work and similarly to the modelling of the drag force on yawed cylinders by Taylor (1952), we approximate the pressure drag on a beam in a potential flow with a conservation of momentum argument. We assume that the flow produces a force proportional to the momentum it carries in the direction perpendicular to the beam. Upon setting this drag force on a beam element equal to the shear force per unit length in a Euler–Bernoulli beam, we obtain

$$EI\frac{\partial^3\theta_j}{\partial S_j^3} = -\frac{1}{2}\rho d C'_D[U_j(S_j)\sin\theta_j]^2, \tag{4}$$

where C'_D is the drag coefficient of one beam inside the porous ball and where the velocity $U_j(S_j)$ perceived by beam j is not assumed constant, i.e., it varies along the beam since the part of the beam closer to the exterior of the ball sees higher flow speed than the part of it deep inside the middle of the ball (Fig. 11(b)). We neglect the contacts between the beams so the only coupling between the deformations of the N beams comes from the flow.

From Newton's third law, the force produced by the beams on the flow can be written similarly. Every element δS_j of beam j creates a force perpendicular to itself on the fluid

$$f_j(S_j) = \frac{1}{2}\rho d C'_D U_j^2 \sin^2\theta_j \delta S_j. \tag{5}$$

The system has a high number of degrees of freedom, since the number of beams N is of the order of 1000 and each beam has a continuous deformation along its length. Moreover, the flow through the multiple beams is complex. Rather than modelling all these degrees of freedom and this complexity of the flow, we use a homogenisation approach similar to Py et al. (2006) and Favier et al. (2009). We consider the ball of beams as a poroelastic continuous media. Deformation of beam j, $\theta_j(S_j)$, becomes a continuous function in Θ, i.e., $\theta(S,\Theta)$. By neglecting gravity, deformation of the system can be considered axisymmetric in φ. We can thus rewrite Eq. (4) as

$$EI\frac{\partial^3\theta}{\partial S^3} = -\frac{1}{2}\rho d C'_D[U\sin\theta]^2, \tag{6}$$

where U and θ are functions of Θ and S.

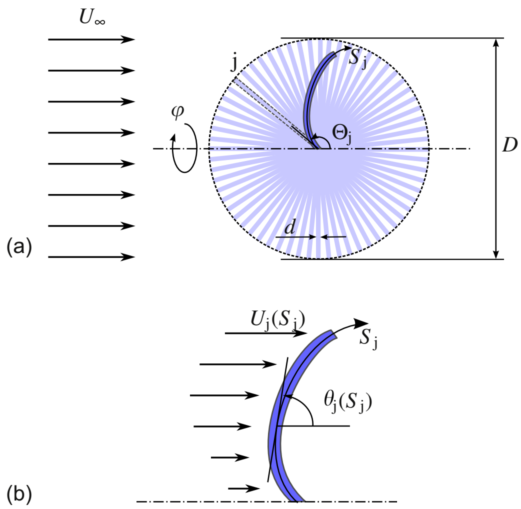

Fig. 11. (a) Schematic diagram of the poroelastic system modelled. (b) Detail of the deformation of beam j part of the system along with the flow the beam perceives.

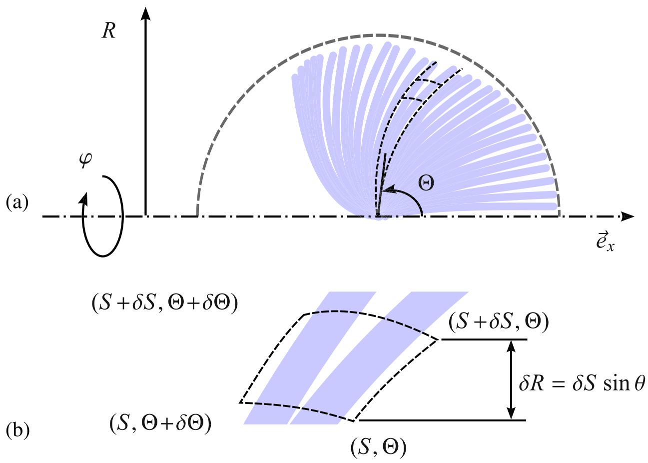

Fig. 12. (a) Schematic diagram of the deformation of the system and (b) detail of the section of a volume element $\delta\Omega$ of the poroelastic continuum.

Homogenisation in space allows to model the forces that the beams exert on the flow as a body force. In a volume $\delta\Omega$ of an element $\delta S\delta\Theta\delta\varphi$, as drawn in Fig. 12, are located $N_\Omega = N\sin(\Theta)\delta\Theta\delta\varphi/4\pi$ beams and the body force they exert on the fluid is N_Ω times the force of one beam element from Eq. (5), i.e.,

$$f(S,\Theta) = \left(\frac{N}{4\pi}\sin\Theta\delta\Theta\delta\varphi\right)\left(\frac{1}{2}\rho d C_D' U^2 \sin^2\theta\delta S\right). \tag{7}$$

In the spirit of keeping the model simple, we make the approximation that the flow is always parallel to the axis of axisymmetry of the system and neglect the transverse component, i.e., $\vec{U}_j = U_j\vec{e}_x$. It follows from this simplification that the flow can be solved with the Bernoulli equation.

For purely axial flow, the fluid in the volume $\delta\Omega$ (Fig. 12) flows trough the surface $R\delta R\delta\varphi$, where R is the eulerian coordinate measured perpendicular to the axis of axisymmetry. From the transformation $\delta R = \delta S\sin\theta$, we can write the loss of pressure due to drag across the volume $\delta\Omega$ as

$$\Delta P = \frac{f\sin\theta}{R\delta R\delta\varphi}. \tag{8}$$

To find the loss of velocity on a variation $\delta\Theta$, we apply Bernoulli's law, $\frac{1}{2}\rho U^2(R,\Theta) = \frac{1}{2}\rho U^2(R,\Theta+\delta\Theta) - \Delta P$:

$$U^2(R,\Theta) - U^2(R,\Theta+\delta\Theta) = -U^2(R,\Theta+\delta\Theta)\frac{N\sin\Theta\delta\Theta C_D' d\sin^2\theta}{4\pi R}. \tag{9}$$

If the angle $\delta\Theta$ is small, Eq. (9) takes the form of a derivative

$$\frac{\partial U}{\partial\Theta} = U\frac{N\sin\Theta C_D' d\sin^2\theta}{8\pi R}. \tag{10}$$

The beam located at $\Theta = \pi$ encounters an unperturbed flow U_∞. For $\Theta < \pi$, since the deformation of the beam varies with R, the local flow velocity is a function of R.

The drag force of the entire poroelastic system is the integral over its volume of the axial component of the body force of Eq. (7):

$$F = \int_0^\pi \frac{N}{2}\sin\Theta \int_0^{D/2} \frac{1}{2}\rho d C_D' U^2(R,\Theta)\sin^3\theta \, \mathrm{d}S \, \mathrm{d}\Theta. \tag{11}$$

To write the problem in a dimensionless way, we define the dimensionless lagrangian and eulerian coordinates, the velocity, the surface density, as well as the reconfiguration and Cauchy number

$$s = \frac{2S}{D}, \quad r = \frac{R}{D}, \quad \overline{U} = \frac{U}{U_\infty}, \quad \eta = \frac{2Nd}{\pi D}, \tag{12}$$

$$\mathcal{R} = \frac{F}{\frac{1}{8}\rho\pi D^2 C_D U_\infty^2}, \quad \widetilde{C_Y} = C_D\frac{\rho D^3 U_\infty^2 d}{16EI}, \quad c = \frac{C_D'}{C_D},$$

where the reference drag of a rigid porous system is defined based on the *macroscopic* drag coefficient of the entire system C_D which is different from the *microscopic* drag coefficient of only one beam inside the ball C_D', and where c is the ratio of both coefficients.

With the parameters of Eqs. (12), Eqs. (6), (10) and (11) are made dimensionless:

$$\frac{\partial^3 \theta}{\partial s^3} = -c\widetilde{C_Y}\overline{U}^2 \sin^2\theta, \tag{13}$$

$$\frac{\partial \overline{U}}{\partial \Theta} = \overline{U}\frac{\eta C'_D \sin\Theta \sin^2\theta}{16r}, \tag{14}$$

$$\mathcal{R} = \frac{\eta c}{2}\int_0^{\pi} \sin\Theta \int_0^1 \overline{U}^2 \sin^3\theta \, \mathrm{d}s \, \mathrm{d}\Theta. \tag{15}$$

Note that we define the Cauchy number, $\widetilde{C_Y}$, based on the macroscopic drag coefficient of a rigid equivalent porous ball, C_D, although it is the drag coefficient of a single filament composing the ball, C'_D, that appears in Eqs. (6) and (10). We do so because C'_D is difficult to measure experimentally.

The dimensionless boundary conditions can be written as follows:

$$\overline{U}|_{\Theta=\pi} = 1, \quad \theta|_{s=0} = \Theta, \quad \left.\frac{\partial \theta}{\partial s}\right|_{s=1} = 0, \quad \left.\frac{\partial^2 \theta}{\partial s^2}\right|_{s=1} = 0. \tag{16}$$

To solve the system of Eqs. (13) and (14), the deformation of the poroelastic media $\theta(s,\Theta)$ and the velocity of the fluid $\overline{U}(r,\Theta)$ are discretised in Θ over N_Θ *reference* beams similarly to Favier et al. (2009). The deformation of the beam furthest upstream at $\Theta=\pi$ is solved first since it perceives an unperturbed flow velocity. Eq. (13) is integrated numerically using the shooting method and the Runge Kutta algorithm. Once the deformation of this beam is known, Eq. (14) is solved at N_r points on r between 0 and 1 to yield the flow perceived by the second reference beam. The equation of deformation (13) is subsequently integrated numerically with Runge Kutta using an iterative scheme since the flow velocity profile is defined in eulerian coordinates and the deformation of the beam is defined in lagrangian coordinates. Once the shape of the beam is found, the loss of momentum in the flow is computed using Eq. (14) and the process is repeated for every reference beam. We finish by solving Eq. (15) to find the reconfiguration number.

Note that care has to be taken when discretising Eq. (14) to insure physically meaningful computations. In its discretised form, it is written as

$$\overline{U}(r,\Theta-\delta\Theta) = \overline{U}(r,\Theta)\left(1-\delta\Theta\frac{\eta C'_D \sin\Theta \sin^2\theta}{16r}\right). \tag{17}$$

When the poroelastic system is dense enough, i.e., when η is large, the term in the parenthesis could become negative over part of r especially close to the centre of the system ($r=0$). Since the lowest value of r where Eq. (17) is evaluated is at $r=\delta r/2$, we can insure that it is always physical if δr is chosen such that $\delta r \geq \eta C'_D \delta\Theta/8$.

Also, when many equilibrium positions exist for a beam, we select the one for which the free end is the furthest downstream. No stability analysis is performed on the different positions, but we judge that this position has the most chance of minimising the potential energy.

The geometry we model is slightly different from that of our experiments because we neglect to model the rigid core of the poroelastic system. Considering that all the coupling between the deformation of the beams comes from the flow and considering the simplicity of the flow model, the effect of the core is neglected. Moreover, by defining the Cauchy number based on the flexible length of the filaments ($D/2-D_i/2$ in Eq. (3) and $D/2$ in Eq. (12)), the model can be appropriately compared with the experiments.

3.2. Theoretical results

To realise the simulations, it was necessary to provide a value for the microscopic drag coefficient C'_D which we could not measure experimentally. The model was thus used to simulate the drag of the rigid specimen tested experimentally and the value of C'_D was calibrated to make the resulting simulated macroscopic drag coefficient C_D match that measured experimentally on the rigid specimen. A value of $C'_D=0.3$ was thus used for the remainder of the simulations.

The first and the second poroelastic specimens tested in the wind tunnel which have, respectively, surface densities of $\eta=6.1$ and $\eta=9.2$ where modelled using $N_\Theta=480$ reference beams. The deformation of the first specimen is shown in Fig. 13. The deformation is qualitatively very similar to that observed in the wind tunnel in Fig. 5.

The reconfiguration curves predicted by the theoretical model of Eqs. (13)–(15) with $\eta=6.1$ and 9.2 corresponding, respectively, to the first (solid line) and second (dash line) specimens are shown in Fig. 9 for comparison with the first (•) and second (◦) experimental specimens. The general trend of the theoretical curves is the same as for the experimental points.

As the model succeeds in reproducing the experimental results in Fig. 9, we use it to investigate the effect of surface density on the reconfiguration. In Fig. 14, the curves of $\mathcal{R}$ versus $\widetilde{C_Y}$ in (a) and versus the ratio $\widetilde{C_Y}/\eta$ in (b) are plotted for a wide range of surface densities. In (a), the curves from left to right represent systems with surface densities of $\eta=0.064$, 0.64, 6.4 and 64; in (b) they go from right to left. In (a) the curves are evenly spread on the logarithmic plot, while in (b), they are made to coalesce at one point about $\widetilde{C_Y}/\eta \approx 3$. This shows that the drag reduction of the poroelastic system studied becomes significant when the Cauchy number spread over every element composing the system is effectively of

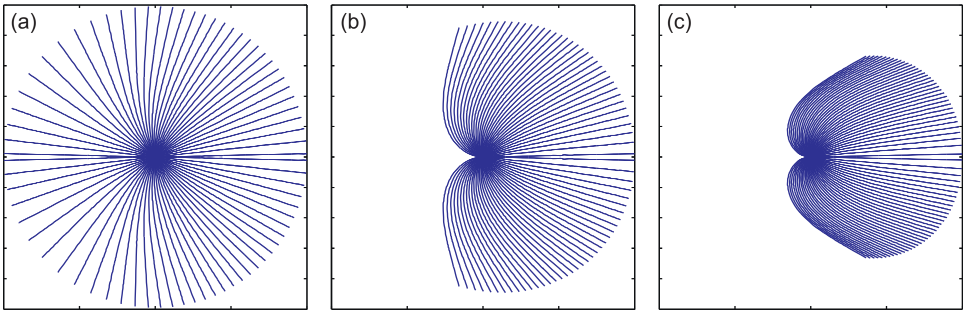

Fig. 13. Visualisation of the modelled deformation of a poroelastic system equivalent to the first specimen subjected to a flow with (a) $\widetilde{C_Y} = 2.8$; (b) 20.6; and (c) 87.2. Note that the Cauchy numbers correspond to the conditions of Fig. 5.

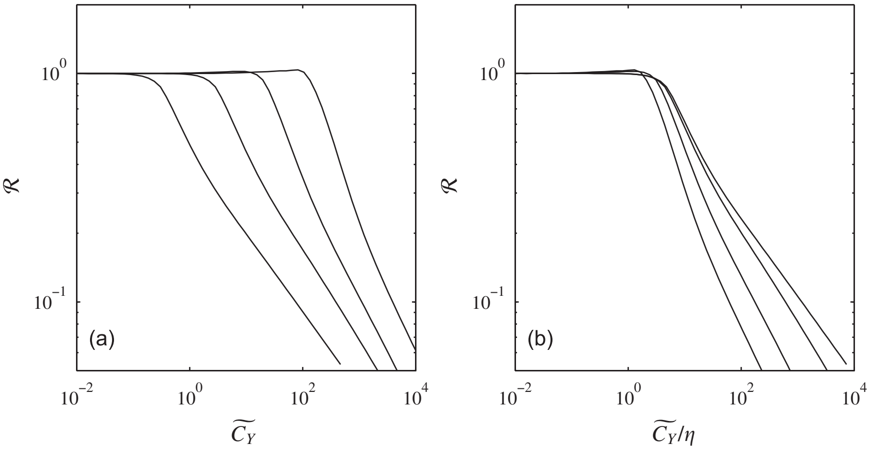

Fig. 14. Effect of the surface density on the reconfiguration curve for poroelastic systems in function of: (a) $\widetilde{C_Y}$, and (b) $\widetilde{C_Y}/\eta$. The curves have surface densities of $\eta = 0.064$, 0.64, 6.4 and 64 from left to right in (a) and from right to left in (b).

order 1, i.e., $\widetilde{C_Y}/\eta \sim \mathcal{O}(1)$. The reconfiguration curve of a poroelastic system can thus be compared with that of a simple system by dividing the Cauchy number by the surface density as is done for the experimental measurements on slender filaments and plates in Fig. 10(b).

At a given Cauchy number on Fig. 14(a), less reconfiguration occurs for the high surface density ball because the aerodynamic load is split onto many more beams and thus does not deform the beams as much. However, at a fixed value of $\widetilde{C_Y}/\eta$ on Fig. 14(b), the reconfiguration number is smaller for the ball with the higher surface density as the aerodynamic load per beam is the same for each ball and the beams of the higher surface density ball benefit from more sheltering.

The curves of Fig. 14(b) coalesce at small values of $\widetilde{C_Y}/\eta$, but at high values when the deformation is large, they have different slopes. Recall that this slope is equal to half the value of the Vogel exponent $\mathcal{V}$. In Fig. 15, the value of Vogel exponent computed at $c\widetilde{C_Y} = 10^4$ is plotted in function of the surface density.

On this graph, a small value of $\eta C_D'$ corresponds to the case where the beams composing the poroelastic system are thin and few. Therefore, they do not perceive the presence of their neighbours through the flow. Accordingly, at $\eta C_D' = 10^{-4}$, the poroelastic system has a Vogel exponent of $\mathcal{V} = -0.6667$ which corresponds to the asymptotic regime of large deformation of plates, filaments and fibres.

However, when $\eta C_D'$ is larger, the system has more drag-generating surfaces and the downstream beams feel a fluid flow altered by the upstream beams. This has an effect on the value of Vogel exponent in the large deformation regime. The Vogel exponent changes from $\mathcal{V} = -2/3$ at low $\eta C_D'$ to a value close to -1 at large values of surface density. For values of $\eta C_D'$ between 3.9 and 64, the Vogel exponent varies only slightly from -0.96 to 1.03. This range of values of $\eta C_D'$ encompasses the two experimental specimens tested. What the model predicts is that if one of the experimental specimens had 2 times less or 10 times more filaments, its Vogel exponent at large $c\widetilde{C_Y}$ would have been approximately the same around $\mathcal{V} \approx -1$.

Similarly as for the flat plates and the filaments in the flow, a dimensional analysis can be performed to obtain the scaling of the drag of the porous system in the large deformation regime assuming that the surface density is very high. As for the filaments, we assume that the original length scale D of the poroelastic system becomes irrelevant as the structure

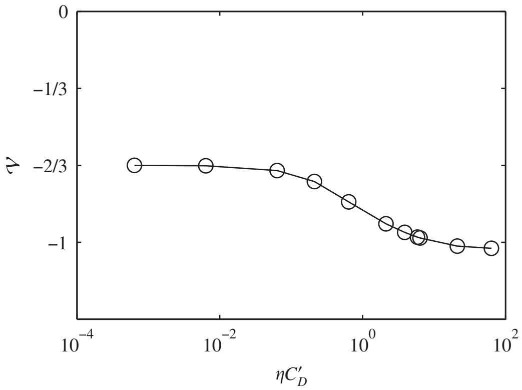

Fig. 15. Variation of the Vogel exponent of the drag of a poroelastic system with surface density. The exponent $\mathcal{V}$ is computed at $c\widetilde{C_Y} = 10^4$.

is highly deformed. Moreover, if the surface density η is large, the exact size of the elements of the poroelastic system is not important. Because the flow through the porous system will lose all of its momentum, the size of the filaments does not matter. Directly behind the poroelastic body, the flow velocity is null. For both large deformations and large surface density, the physical problem of the reconfiguration of this 3-D poroelastic body is described by four quantities:

$$F\,[\mathrm{N}],\quad EI\,[\mathrm{N\,m^2}],\quad U_\infty\,[\mathrm{ms^{-1}}],\quad \rho\,[\mathrm{kg\,m^{-3}}].$$

The one dimensionless number required to describe this problem is thus

$$\frac{F}{(EI\rho)^{1/2}U}.$$

Accordingly, the drag on a poroelastic system in the large deformation regime should obey a Vogel number of $\mathcal{V} = -1$. Again, this is the value observed on Fig. 15 at large values of $c\widetilde{C_Y}$.

4. Conclusion

By performing the first experiments on the reconfiguration of synthetic poroelastic systems, it was shown that the drag on these systems is characterised by the Cauchy number, the reconfiguration number and the surface density.

The drag of the synthetic poroelastic system studied shows particularities similar to those of real trees. As measured on branches of Loblolly Pine and American Holly by Vogel (1984), the drag on the poroelastic system was measured to increase in a more pronounced way than a U^2 law because the upstream filaments realign themselves in the flow.

A model based on a conservation of momentum in the direction of the flow coupled with the large deformation Euler–Bernoulli equation of many beams allows to predict the reconfiguration of the specimens tested experimentally. The same model shows that for increasing surface density, the large deformation-regime Vogel exponent transitions from the $-\frac{2}{3}$ value of the 2-D reconfiguration of a slender structure to the -1 value of a volumetrically homogeneous poroelastic body. The question thus arises of what would happen to the reconfiguration of a 2-D poroelastic body such as a hairy cylinder. Also, the scaling law in $\mathcal{V} = -1$ at large surface density and Cauchy values exists for wide range of values of surface density. This scaling can be predicted from dimensional analysis by assuming that the original size of the poroelastic body as well as the size of drag-creating elements play no role in the problem.

On the scaling law for poroelastic bodies, it is worth mentioning that in the literature, almost all the Vogel exponent values we found for coniferous trees are about -1 (Vogel, 1984; Mayhead, 1973; Rudnicki et al., 2004). Moreover, these trees have a structure that somewhat resembles that of the poroelastic system studied here. Like the balls made of filaments, coniferous trees are poroelastic structures made of lots of beams which create drag: long thin needle-like foliage. It might not be a coincidence that 4 out of 5 of the Vogel exponents we found in the literature for coniferous trees are about -1. It would be interesting to evaluate the surface density of these species and to test specimens using the same experimental protocol used here for synthetic specimens. This would allow for better understanding of why there seems to be an homogeneity in the values of Vogel exponents in the literature. Also, getting an estimate of the Cauchy numbers encountered by trees and other plants could help bridge the gap between fundamental physics/mechanics studies and the biology/botany ones.

Another possible avenue for future work on vegetation drag could investigate how plants strike the right balance in structural flexibility. With the right structural flexibility, plants reduce their drag through passive reconfiguration. However, it is well known that the drag on flexible structure increases significantly upon the onset of flutter (Morris-Thomas and Steen, 2009). How should a flexible structure be designed to maximise its reconfiguration while avoiding flutter?

Acknowledgements

The authors acknowledge Pascal Hémon for designing and building a high quality experimental set-up. We acknowledge the financial support of the 'Fonds québécois de la recherche sur la nature et les technologies', École Polytechnique and the ANR Program 06-BLAN-0210 'Chêne-Roseau' involving INRA, INRIA and École Polytechnique.

References

Alben, S., Shelley, M., Zhang, J., 2002. Drag reduction through self-similar bending of a flexible body. Nature 420, 479–481.
Alben, S., Shelley, M., Zhang, J., 2004. How flexibility induces streamlining in a two-dimensional flow. Physics of Fluids 16, 1694–1713.
Baker, C., 1995. The development of a theoretical model for the windthrow of plants. Journal of Theoretical Biology 175 (3), 355–372.
Boizard, S.D., Mitchell, S.J., 2009. Resistance of red mangrove (*Rhizophora mangle* l.) seedlings to extraction. In: Proceedings of the Sixth Plant Biomechanics Conference, Cayenne, French Guyana, France, pp. 110–115.
Cermak, J., Isyumov, N., 1998. Wind Tunnel Studies of Buildings and Structures. American Society of Civil Engineers.
Chakrabarti, S., 2002. The Theory and Practice of Hydrodynamics and Vibration. Singapore, World Scientific.
de Langre, E., 2008. Effects of wind on plants. Annual Review of Fluid Mechanics 40, 141–168.
Dupont, S., Brunet, Y., 2006. Simulation of turbulent flow in an urban forested park damaged by a windstorm. Boundary-Layer Meteorology 120 (1), 133–161.
Dupont, S., Gosselin, F., Py, C., de Langre, E., Hemon, P., Brunet, Y., 2010. Modelling waving crops using large-eddy simulation: comparison with experiments and a linear stability analysis. Journal of Fluid Mechanics 652, 5–44.
Favier, J., Dauptain, A., Basso, D., Bottaro, A., 2009. Passive separation control using a self-adaptive hairy coating. Journal of Fluid Mechanics 627, 451–483.
Gosselin, F., 2009. Mécanismes d'Interactions Fluide-Structure Entre Écoulements et Végétation. Ph.D. Thesis, École Polytechnique, Palaiseau. France.
Gosselin, F., de Langre, E., Machado-Almeida, B., 2010. Drag reduction of flexible plates by reconfiguration. Journal of Fluid Mechanics 650, 319–342.
Harder, D., Speck, O., Hurd, C., Speck, T., 2004. Reconfiguration as a prerequisite for survival in highly unstable flow-dominated habitats. Journal of Plant Growth Regulation 23, 98–107.
Koehl, M.A.R., Alberte, R.S., 1988. Flow, flapping, and photosynthesis of nereocystis leutkeana: a functional comparison of undulate and flat blade morphologies. Marine Biology 99 (3), 435–444.
Mayhead, G., 1973. Some drag coefficients for British forest trees derived from wind tunnel studies. Agricultural Meteorology 12, 123–130.
Moe, H., Fredheim, A., Hopperstad, O., 2010. Structural analysis of aquaculture net cages in current. Journal of Fluids and Structures 26 (3), 503–516.
Morris-Thomas, M., Steen, S., 2009. Experiments on the stability and drag of a flexible sheet under in-plane tension in uniform flow. Journal of Fluids and Structures 25 (5), 815–830.
Niklas, K.J., 1991. The elastic moduli and mechanics of *Populus tremuloides* (salicaceae) petioles in bending and torsion. American Journal of Botany 78 (7), 989–996.
Py, C., de Langre, E., Moulia, B., 2006. A frequency lock-in mechanism in the interaction between wind and crop canopies. Journal of Fluid Mechanics 568, 425–449.
Ricciardi, G., Bellizzi, S., Collard, B., Cochelin, B., 2009. Modelling pressurized water reactor cores in terms of porous media. Journal of Fluids and Structures 25 (1), 112–133.
Rudnicki, M., Mitchell, S.J., Novak, M.D., 2004. Wind tunnel measurements of crown streamlining and drag relationships for three conifer species. Canadian Journal of Forest Research 34, 666–676.
Schouveiler, L., Boudaoud, A., 2006. The rolling up of sheets in a steady flow. Journal of Fluid Mechanics 563, 71–80.
Shelley, M.J., Zhang, J., 2011. Flapping and bending bodies interacting with fluid flows. Annual Review of Fluid Mechanics 43 (1), 449–465.
Taylor, G., 1952. Analysis of the swimming of long and narrow animals. Proceedings of the Royal Society of London. Series A, Mathematical and Physical Sciences 214 (1117), 158–183.
Vogel, S., 1984. Drag and flexibility in sessile organisms. American Zoologist 24 (1), 37–44.
Vogel, S., 1989. Drag and reconfiguration of broad leaves in high winds. Journal of Experimental Botany 40, 941–948.
Vogel, S., 1996. Life in Moving Fluids, second ed. Princeton University Press, Princeton, NJ.